Sparse Phase Portrait Analysis for Preprocessing and Segmentation of Ultrasound Images of Breast Cancer

Sirikan Chucherd and Stanislav S. Makhanov

Abstract—Computer aided diagnostics of the breast cancer is one of the most challenging problems of the contemporary medical image processing. Computerized detection of the breast tumors from ultrasound (US) images provides the way which helps the physicians to decide whether a certain solid tumor is benign or malignant. However, it is one of the most difficult types of images to assess.

We propose a new method to improve the accuracy of the tumor detection based on phase portrait analysis (PPA) applied at the preprocessing stage. The PPA works on the image gradient vector field. The algorithm detects patterns resembling standard linear flow configurations and classifies them as the noise, the boundary of the tumor or the regular point (background). The PPA is followed by the generalized gradient vector flow procedure (GGVF) and segmentation by active contours (snakes). Standard methods such as conventional filters and clustering are also included in the preprocessing scheme.

We present and compare several versions of the method. The first version is a combination of PPA and multiresolution analysis (MRA). The second version called sparse phase portrait analysis (SPPA) includes clustering and subsampling.

The PPA has been tested with a rule based, linear and exponential classifier. The preprocessing sequence includes the Gaussian, median and despeckling filters, fuzzy C mean clustering (FCM) and region growing (RG).

The approach has been tested with a series of real US breast tumor images. The results are compared with the ground truth hand-drawn by the radiologists.

The numerical experiments show that GGVF endowed with MRA and PPA over performs the conventional GGVF snakes. The SPPA is faster and easier to implement. However, it needs to be combined with a clustering procedure such as FCM. In this case its efficiency is comparable with GGVF-MRA. The both procedures benefit from additional preprocessing and the continuous linear or exponential classifier.

Index Terms—phase portrait analysis, multiresolution analysis, medical image processing

I. Introduction

THE ultrasound images provide a good criterion to decide whether a certain solid tumor is benign or malignant. High performance computer aided diagnostic systems help the physicians to avoid misdiagnosis and unnecessary biopsy without missing cancers. However, the US images are one of the most difficult types of images to assess and the accuracy of the computer based diagnostics is not always acceptable. It is often difficult to separate the tumor from the background even when the existence of the tumor is evident. Therefore, segmentation of tumors is one of the most important stage in the computer aided US cancer diagnostics.

Among the most promising techniques for extraction of complex objects from digital images are active contours or snakes, originally introduced by Kass et al. [1]. Since the seminal work of Kass and colleagues, techniques based on active contours have been applied to many object extraction tasks with a different degree of success. In particular, snakes have been used to locate objects in various applications of medical image processing such as abnormalities in the images of the human heart, liver, brain, breast, etc [2], [3], [4], [5], [6], [7], [8], [9], [10], [11], [12].

The active contour evolves to minimize the contour energy that includes the internal energy of the contour and the external energy of the image. During the snake deformation, the internal force maintains the contour smoothness, while the gradient-based external force attracts the contour to the desired boundaries in the image. The deformation stops when the snake achieves a minimum of the energy.

The main drawback of the method is that the noise and small objects attract the snake to a local energy minimum, which does not correspond to the actual object. To avoid these effects and to reach the desired boundary, the initial snake should lie close to the object's boundary.

The most important component of the snake techniques is an external force which pushes the snake towards the desired object along the directions of the image gradient vector field.

In order to make it work, the gradients nearby the boundary must be extended so that the snake "feels "the object even when initialized far from it. The problem can be treated by amplifying the outward (or inward in case of contracting snakes) force. Examples are balloons (artificially inflated contours) [13] and distance snakes [14]. The external force field for the distance snake is constructed as the negative of the external energy gradient, which is the distance from each point to its closest edge points in the image. Consequently, the initial contour can be located far away from the desired boundary if there are no spurious edges along the way.

Many modifications such as the "stop and go " snakes [15], multi-direction snakes [16], gravitation force snakes [17], watershed-balloon snakes [18], balloon snakes combined with nonlinear filtering [19] are based on similar ideas. The image force is modified or altered to increase the capture range and decrease the sensitivity to the possible noise, shadows and (in case of the medical images) obstructing structures and tissues.

Another group of methods is based on minimization of the energy subject to a certain conditions improving the

convergence and accuracy. Sectored snakes [20] deform the contour subject to constraints derived from an priori knowledge of the object shape, extracted from the training set of images. Fourier type descriptors have been used in [21] to evolve the curve to a prescribed shape defined by a template. The prior information is introduced through a set of invariants (translation, rotation and scaling) computed using the Fourier Transform.

Furthermore, the force can include not only the edge based features but region based features as well (for instance the homogeneity of the enclosed region). The region-based features can be combined with edge-based features incorporated in the external forces [22], [23].

Starting from multiple seeds, [24] performs segmentation of the entire image by iterative boundary deformation and region merging.

The so-called T-snakes [25] and their improvements such as the dual T-snakes [26] based on iterative re-parameterization of the original contour are able to make the use of the self loops. However, the approach allows only "rigid" deformations limited by the superimposed "simplicial grid". An intrinsic internal force that does not depend on contour parameterization based on regularized contour curvature profile has been proposed in [27], [28]. An interesting geometric technique based on exploiting the snake's loops is presented in [29].

A competing approach called the level set method [30] is based on the ideas of Osher and Sethian [31] to use a model of propagating liquid interfaces with curvature-dependent speeds.

The level set method combined with the contour energy minimization resulted in a variety of the so-called geodesic deformable models [32], [33], [34], [35].

However, the level set method makes it difficult to impose arbitrary geometric or topological constraints on the evolving contour via the higher dimensional surface [25]. Besides, the level set models may generate shapes having inconsistent topology with respect to the actual object, when applied to noisy images characterized by large boundary gaps [36]. Li et al. [37], in reference to the problem of topological adaptation and computational complexity write "in light of the . . . inherent weaknesses of geometric active contour models, it is worthwhile to seek solutions within the parametric model realm".

Rochery et al. propose a parametric model for higher-order active contours, in particular, quadratic snakes, for extraction of linear structures like roads or blood vessels [38]. The idea is to use a quadratic formulation of the contour's geometric energy to encourage anti-parallel tangents on opposite sides of the vessel and parallel tangents along the same side of the vessel. These priors increase the final contour's robustness to partial occlusions, decrease the likelihood of false detections in regions not shaped like vessels, and help to prevent self-looping.

Further improvements lie along the lines of processing the underlying vector field rather then modifying the snake model itself. A number of popular codes are based on a gradient vector flow (GVF) method proposed by Prince and Xu [39], [40]. A "raw" gradient vector field derived from the image gray level is replaced by a field which minimizes a certain variational functional. The functional is designed to extend the large gradients far from the boundary, smooth noise and speckles while keeping gradients attached to strong edges. The corresponding Euler equations represented by linear elliptic PDEs are solved numerically. The initial condition for these PDEs is the "raw" gradient vector field. The solution is interpreted as the steady state representation of a non-stationary diffusion process with constant coefficients.

The generalized gradient vector flow (GGVF) [41] extends the GVF method by introducing a non-uniform diffusion. The GGVF is defined as a steady state solution of a system of parabolic equations with the elliptic terms and the source term similar to the GVF model. However, the GGVF employs space-dependent diffusion which provides better segmentation accuracy and a larger capture range.

Some variations of these ideas are the multidirectional GGVF [16] and the non-linear diffusion method [42].

However, GGVF combined with an appropriate noise removal routine remains one of the most popular choices. Numerous research papers apply GGVF active contours to medical images. The examples are multi-direction snakes for skin cancer camera images [16], topology-adaptive snakes for MR brain images and CT scans [25], gravitational force snakes for a variety of medical and non-medical images [17], narrow-band snakes for MRI and CT scan images of lungs [43], distance snake, GVF snake, balloon snake, "area and length" snakes, geodesic snakes, constrained snakes and level set method for MRI, CT and US images of brain, liver and kidney [35], region-competition snakes (originally proposed in [24]) for CT scan slices of arteries [44], sectored snakes for abdominal CT scans[20], parametric snakes for US of breast masses [45], 3D-snakes for US breast cancer images [9], [10], GVF snakes with edge map pre-processing for US of the kidney tumors [11], GVF snakes combined with region growing and the median filter for US breast tumors [12], sketch-snakes for chest X-Ray images [46], combination of snakes and the active shape models for US of the human heart [47], the "early-vision"/discrete-snake model for a variety of the US images [48], multi-resolution snake for echographic and echobrachial images [49], GGVF snakes combined with a continuous force field analysis for breast tumor US images [50] and GGVF snakes combined with a multiresolution PPA [51] for segmentation of the breast tumors on US images.

The success of such segmentations critically depends on preprocessing. It is often more important than the efficiency of the active contour method. However, only a few papers dealing with the snakes analyze preprocessing for the US imagery. The Gaussian, mean and median filters [52], Gabor filters [48] and speckle noise filters [53], [54] are among the most popular preprocessing steps.

Furthermore, more often than not, preprocessing is a well arranged sequence of operations including (but not limited to) filtering, morphological transformations and edge detection procedures specific for the particular type of medical imagery. It is clear that this sequence depends on the subsequent segmentation method, that is, some preprocessing sequences are better suited for snakes than others.

A combination of region growing and median filtering is proposed for the GGVF snakes in [12]. A single run of the anisotropic diffusion filter (non-linear filter [55]) is proposed for the multi direction snake [16]. Non-linear filters applied

to the GVF vector field (rather than to the original image) are discussed in [56]. A curvature diffusion filter is proposed in [57] as a preprocessing step for the level set method.

A human operator is employed to initialize the snake close enough to the actual boundary [58]. Similar interactive medical image segmentation (sketch snakes) is introduced in [46]. Other preprocessing operations such as the edge detection and filtering can be controlled by a human operator as well. However, the snake, the GGVF, the edge detection and the initialization require many parameters to adjust. Therefore, training the operator is a non-trivial task.

A preprocessing [59], [60] for density-based segmentation with snakes employs histogram adjustment, noise reduction using iterative dilation and median filtering. The noise reduction is followed by evaluation of the layer of interest using the Fuzzy C-Mean (FCM) clustering. A rough watershed object localization is followed by a fine snake based segmentation. Algorithm [59] has been applied to the polycystic ovary ultrasound images.

Popular noise removal filters include the Gaussian, the median and a despeckling filter, such as the Lee filter [61]. However, a variety of other filters has been successfully applied to the US images. For instance, [62] compares nine filters applied to despeckle the US images and [52] considers ten types of the despeckling filters. A fusion of the median and the Wiener filter is combined with the despeckling Frost filter [63] and a contrast adjustment technique in [64]. A tree-structured nonlinear filter and special types of wavelet transforms have been proposed in [65] for the transrectal ultrasound. A combination of filtering, edge map and initialization by a human operator [12] employs an iterative truncated median filter to reduce the speckle noise. Histogram equalization followed by a morphology operation displayed promising results for the US breast images [66]. In [67] the speckle noise is suppressed by the anisotropic diffusion filter [68] and the stick filter [69].

In summary, preprocessing of the US images for a subsequent segmentation by snakes is important. The preprocessing steps are versatile and there is no agreement which method is the best. An efficient preprocessing is a well arranged sequence of operations which includes (but not limited to) filtering, clustering, morphological transformations and edge detection procedures.

This paper introduces a new preprocessing method based on phase portrait analysis (PPA). The PPA detects linear flow configurations and classifies them as the noise, the boundary of an object or the regular point (background). The method employs the standard linear flow classification (Fig.1) applied to the corresponding gradient vector field. The boundary of the object is represented by the node-saddle. The noise corresponds to an attracting star, repelling star, attracting node and repelling node (Fig.1).

It should be noted that in the past PPA was applied to a variety image processing applications such as, satellite imagery [70], texture analysis [71], and the fingerprint identification [72]. In medical image processing PPA applied to detect abnormalities in mammogram breast tumor images [73]. However, to the best of our knowledge, the idea of PPA in the context of GGVF active contours has been overlooked.

PPA is based on a numerical measure of a strong edge, applied in a rotating window of a varying size. This part of
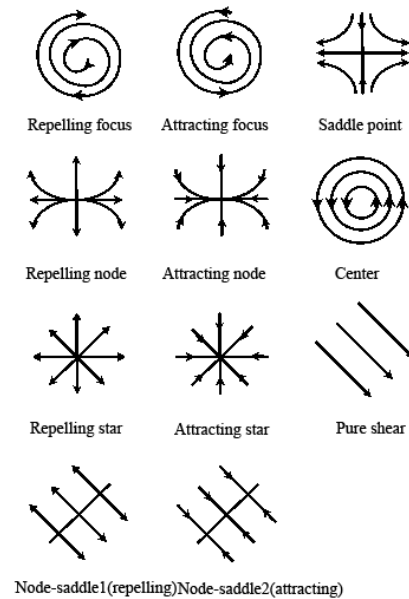

Fig. 1.   Phase portrait linear flow pattern

the algorithm is similar to oriented filtering (the oriented Gabor filter, the oriented LoG filter, etc). However, the proposed method differs from the conventional filters. The PPA produces a score which measures the similarity of the vector field in the particular window to standard linear flow patterns. The patterns are characterized by eigenvalues of the corresponding linear flow matrix. Recall that the boundary configuration is represented by the attractive or repelling line (node saddle case I and II, see Fig.1) and the noise is represented by the attracting or repelling stars. Since the gradient vector field is rotation-free, the local flow is limited to above patterns whereas patterns "focus" and "center" do not appear. Finally, the repelling and attracting nodes may represent the boundary as well as the noise. The elongated node characterized by a small ratio of the eigenvalues represents the boundary but a round node with a large ratio corresponds to the noise.

We compare several versions of the method. The PPA has been tested with a rule based, linear and exponential classifier. The classifiers depend on the ratio of the corresponding eigenvalues of the linear flow matrix.

The preprocessing sequence includes the Gaussian, median and speckle filters, multiresolution analysis and subsampling (sparse PPA) combined with suitable clustering procedures.

The approach has been tested with a series of real US breast tumor images. The results are compared with the ground truth hand-drawn by the radiologists. The numerical experiments show that GGVF endowed with PPA over performs conventional GGVF snakes.

We also show that combining a sequence of selected preprocessing procedures with the PPA always provides an accuracy increase.

Finally, PPA can be integrated into the GGVF iterations (steps along the pseudo-time) to construct improved edge maps similarly to the continuous force field analysis [50].

However, this option is computationally expensive and lies out of the scope of this paper.

II. GENERALIZED GRADIENT VECTOR FLOW SNAKES

An active contour or snake is a curve $X(s) = (x(s), y(s)), s \in [0,1]$, evolving inside the image so that it attaches itself to the desired object. The evolution of the snake is governed by Euler equations corresponding to an energy functional defined by

$$
\begin{aligned}
E = & \int_0^1 a|X'(s)|^2 + b|X''(s)|^2 ds \\
& + \int_0^1 E_{\text{ext}}(X(s))\, ds,
\end{aligned} \tag{1}
$$

where E_{ext} is an external force which moves the snake towards the object. For instance, it could be a smoothed version of the gradient vector field. The first term establishes an equidistribution of points along the resulting curve whereas the second term ensures against large curvatures. The weighting parameters a and b are to control the snake's tension and rigidity. The minimum of the functional is supposed to be achieved on a curve which approximates the boundary of the object of interest. Although this claim has not been proven theoretically for realistic assumptions such as the presence of noise, false objects, speckles, low contrast areas etc, a strong rationale behind it is variational functional (1).

Popular gradient vector flow techniques (GVF) originally proposed by Prince and Xu [39], [40], replace a gradient vector field E_{ext} derived from the image edges by a new vector field. The new field is obtained by extending the large gradients far from the object boundary and smoothing the gradients caused by noise. The GVF is a minimizer of the following functional

$$
\begin{aligned}
& \mu \iint |\nabla u|^2 + |\nabla v|^2\, dx\, dy \\
& + \iint |\nabla f|^2 |V - \nabla f|^2\, dx\, dy,
\end{aligned} \tag{2}
$$

where μ is the diffusion coefficient. The first integral produces a smoothly varying vector field $V = (u(x,y), v(x,y))$, while the second integral encourages the vector field to approach ∇f, if $|\nabla f|$ is large. The Euler equation for functional (2) is given by

$$
\mu \nabla^2 V - (V - \nabla f)|\nabla f|^2 = 0. \tag{3}
$$

Equation (3) can be solved by treating V as a function of time. The steady-state solution of the corresponding linear parabolic equation

$$
\frac{\partial V}{\partial t} = \mu \nabla^2 V - (V - \nabla f)|\nabla f|^2 \tag{4}
$$

is the desired solution of the Euler equation (3). Equation (4) is discretized with regard to the time and space variables and solved numerically. The time steps are interpreted as numerical iterations.

Xu and Prince [41] extended the GVF technique by introducing spatially varying coefficients to decrease the smoothing effect at the true boundaries, namely,

$$
\frac{\partial V}{\partial t} - g(|\nabla f|)\nabla^2 V - h(|\nabla f|)(\nabla f - V) = 0. \tag{5}
$$

TABLE I
TYPES OF 2D CRITICAL POINTS.

Pattern	Eigenvalues	
Center	$R_1 = R_2 = 0$	$I_1 = -I_2 \neq 0$
Attracting Focus	$R_1 = R_2 < 0$	$I_1 = -I_2 \neq 0$
Repelling Focus	$R_1 = R_2 > 0$	$I_1 = -I_2 \neq 0$
Attracting Node	$R_1 \neq R_2 < 0$	$I_1 = I_2 = 0$
Attracting Star	$R_1 = R_2 < 0$	$I_1 = I_2 = 0$
Repelling Node	$R_1 \neq R_2 > 0$	$I_1 = I_2 = 0$
Repelling Star	$R_1 = R_2 > 0$	$I_1 = I_2 = 0$
Saddle Point	$R_1 > 0, R_2 < 0$	$I_1 = I_2 = 0$
Node-Saddle 1	$R_1 > 0, R_2 = 0$	$I_1 = I_2 = 0$
Node-Saddle 2	$R_1 < 0, R_2 = 0$	$I_1 = I_2 = 0$
Pure Shear	$R_1 = R_2 = 0$	$I_1 = I_2 = 0$

The improved version is called the generalized gradient vector flow (GGVF). The weighting functions g and h depend on the gradient of the edge map so that in the proximity of large gradients g gets smaller whereas h becomes larger. In [41] the following weighting functions have been proposed

$$
g(|\nabla f|) = e^{-|\nabla f|/K}, \quad h(|\nabla f|) = 1 - g(|\nabla f|), \tag{6}
$$

where K is a calibration parameter.

However, even GGVF may produce a vector field, where the gradients are not extended far enough from the actual boundary of the object. On the other hand, the true boundary can be partially or even entirely destroyed by excessive smoothing when K or the time step is too large. The iterations should be interrupted before if happens. However, a conventional stopping criterion based on the proximity to the steady state solution may produce an "over-smoothed" solution. On the other hand interrupting the iterations too early may lead to false boundaries and artifacts. Our practical experiments show that a correct preprocessing may reduce and even entirely eliminate these negative effects.

III. PHASE PORTRAIT ANALYSIS

This section introduces several versions of PPA. The first version is a combination of PPA and multiresolution analysis (GGVF-PPA-MRA) [51]. The second version called sparse phase portrait analysis (GGVF-SPPA) includes clustering and subsampling.

A. Linear flow matrix

Recall that the linear system model represents the underlying vector field V as a solution of a linear system $dv/dt = Av$. Matrix $A = \begin{pmatrix} a & b \\ c & d \end{pmatrix}$ can be obtained by a linear least square method applied in the sampling window to minimize $||V - A \begin{pmatrix} x \\ y \end{pmatrix}||$ with regard to a, b, c and d.

There are eleven basic linear flow patterns characterized by the eigenvalues of the flow matrix (see Table 1) [74], where λ_1, λ_2 are the eigenvalues, $R_i = \text{Re}\lambda_i, I_i = \text{Im}\lambda_i$. Since we apply our classification to the vector field subjected to smoothing and boundary enhancing effects of GGVF. The most prominent patterns are attracting/repelling stars (noise), node-saddle (boundary) and the pure share (regular point).

These configurations can be explained considering a physical analogy with the heat diffusion simulated by Eq.(4) and the resulting vector field. The noise generates an isolated source (sink) of heat. In terms of the corresponding vector
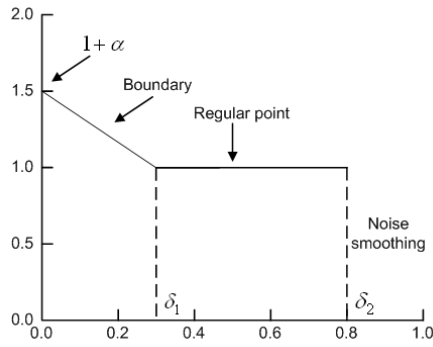
Fig. 2.   Linear function
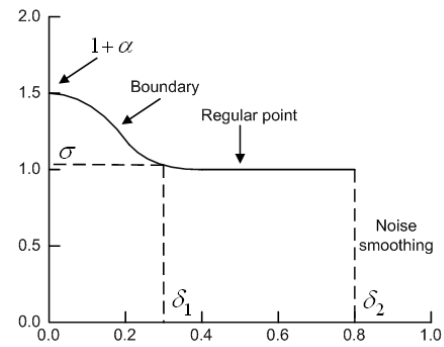
Fig. 3.   Exponential function

field it is an attracting (repelling) star. In turn, a boundary of the object corresponds to a source (sink) distributed along a line or curve. In this case PPA detects an attracting or repelling node-saddle. Finally, a slow varying gray level (background) corresponds to "shear"-type of the vector field.

B. Classifiers

The tumors in the US images of breast are represented by dark spots at the lighter noisy background. Usually, the tumor contains small and large groups of lighter pixels representing the noise. The boundary of the tumor is typically ill-defined, fuzzy and is often hard to evaluate visually.

Consider the most frequent patterns of the vector field: attracting star(noise), attracting saddle (boundary) and the shear (a regular point). Classifier proposed in [51] is given by

$$S(W,p) = \begin{cases} \text{noise, } \Lambda > \Delta_1, \\ \quad |\lambda_1| > \Delta_2 \text{ or} |\lambda_2| > \Delta_2 \\ \text{boundary, } \Lambda \leq \Delta_1, \\ \quad |\lambda_1| > \Delta_2 \text{ or} |\lambda_2| > \Delta_2 \\ \text{regular point,} \\ \quad |\lambda_1| \leq \Delta_2 \text{ or} |\lambda_2| \leq \Delta_2, \end{cases} \quad (7)$$

where

$$\Lambda \equiv \Lambda(\lambda_1,\lambda_2) = \frac{\min(|\lambda_1|,|\lambda_2|)}{\max(|\lambda_1|,|\lambda_2|)},$$

W is the window around pixel p and Δ_1, Δ_2 the thresholds evaluated by training.

When classifier $S(W,p)$ detects the boundary, the gray level is increased by $f_{new} = (1+\alpha)f_{old}$, where α is evaluated by training. In our experiments we consider $\alpha = 0.5$.

We also consider a continuous boundary classifier defined by

$$S_L(W,p) = \begin{cases} ((1+\alpha)(\delta_1 - \Lambda) + \Lambda)/\delta_1, \\ \quad \Lambda \leq \delta_1, \ \lambda_i \neq 0, \ i = 1, 2 \\ 1, \qquad\qquad\qquad \text{otherwise,} \end{cases} \quad (8)$$

where $[0,\delta_1]$ is the range of the boundary points (see Fig.2).

Note that (8) is piecewise linear, however, the function can be easily changed to exponential or trigonometric. For instance, the exponential classifier is defined by

$$S_E(W,p) = \begin{cases} \alpha e^{-\Lambda^2\beta} + 1, \\ \quad \Lambda \leq \delta_1, \ \lambda_i \neq 0, \ i = 1, 2 \\ 1, \qquad\qquad\qquad \text{otherwise,} \end{cases} \quad (9)$$

where

$$\beta = \ln(-\frac{1-\sigma}{\alpha})/\delta_1^2$$

and where σ controls the decay of $S_E(W,p)$ (see Fig.3).

$S(W,p)$ increases the gray level of the edge map if the configuration of the vector field is close to a node-saddle or an attracting node (boundary). For instance, in case of saddle $\Lambda(\lambda_1,\lambda_2) = 0$ the gray level gets increased by multiplying by $1 + \alpha$. It also gets increased when $\Lambda(\lambda_1,\lambda_2) < \delta_1$. As opposed to classifier (7) where the gray level is multiplied by $1 + \alpha$ irrespectively of Λ, classifiers (8) and (9) increase it proportionally. The smaller is Λ the greater is the increase. The gray level transformation is then $f_{new} = S(W,p)f_{old}$.

The noise removal step is similar to that employed by (7), namely, if $\Lambda > \delta_2$ then the intensities in the entire window are replaced by an intensity of the background. For the US images this value is close to zero (black background). Alternatively the median or the Gaussian filter can be applied.

C. Phase portrait with multiresolution analysis

The proposed algorithm combines GGVF-PPA snake with the multiresolution analysis (MRA) based on the Daubechies wavelets D4 [75]. The PPA detects the noise and the boundary points for each multiresolution level and for various size of the window. The first run of PPA detects and removes the noise. The gray level in the corresponding windows gets smoothed. The second run detects the boundary. If the point belongs to the boundary, the gray level in the central point of the window gets increased. Then the gradient vector field is reconstructed and GGVF applies to the improved field. Finally, the snake runs on the resulting vector field until convergence and is interpolated to the higher level. The procedure is repeated until the highest resolution level is achieved. The steps of the algorithm are given below.

1) Apply MRA to the original image (2-3 levels).
2) Set the resolution level to the lowest one.
3) Apply the Canny edge detector to obtain a gray level edge map f_e.
4) Evaluate ∇f_e.
5) Noise removal step:
    a) Select an initial window size.
    b) Smooth the entire window if the central point p of W is classified as the noise.
    c) Increase the window size and go to 5.a until a maximum window size is reached.
6) Evaluate new ∇f_e.
7) Boundary detection step:
    a) Select an initial window size.
    b) Apply PPA boundary detection with classifier $S(W,p)$ or $S_L(W,p)$ or $S_E(W,p)$.
    c) Enhance the gray level at p if it is classified as the boundary.
    d) Increase the window size and go to 7.b until maximum window size is reached.
8) Evaluate new ∇f_e.
9) Run GGVF on the improved ∇f_e.
10) Run the snake on the resulting vector field until convergence.
11) Interpolate the snake to the next resolution level.
12) Set the image to the next resolution level.
13) Go to 3 until the highest resolution level is achieved.

Note that the maximum increase of the gray level is $1+\alpha$. If $f_{new} > 255$ at few points then $f_{new} := 255$ but if $f_{new} > 255$ at many points, the entire image is re-scaled.

D. Sparse phase portrait analysis

This version is based on the idea that subsampling splits the noise into smaller groups which can be easier eliminated by PPA. Of course, the boundary also gets split but if the sampling window is not large the GGVF is still capable of increasing the capture range of the snake and attracting it to the true boundary. We call this version the sparse phase portrait analysis (SPPA).

Subsampling is less computationally expensive then MRA. There is no need to apply a wavelet filter bank and interpolate the snake from one multiresolution level to another. However, subsampling does not eliminate the noise, it is just breaks it into smaller groups. It is also hard to eliminate shadows which may produce "double boundaries" (see Fig. 4(a)). Therefore, SPPA is combined with clustering. First, the gray level image is clustered using a hierarchical fuzzy C mean method or region growing [76]. This enables us to remove some of the double boundaries (see Fig. 4(b)) and to suppress the noise. Next, PPA applies to a window, sliding with the step equal to its size (sparse PPA see Fig. 5). Although, this step is not well justified theoretically, it is out experience that it works well with the US images. Moreover, with an appropriate size of the sampling window, the procedure needs only one run. The steps of the algorithm are given below.

1) Apply FCM clustering to the original image to obtain $f_{clustered}$.
2) Apply the Canny edge detector to $f_{clustered}$ to obtain a gray level edge map f_e.
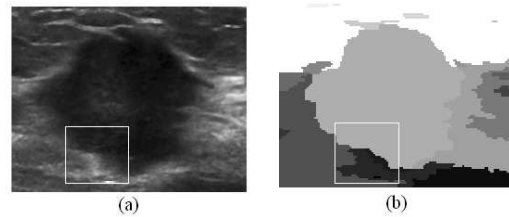
Fig. 4. Double boundaries (a) The original image, (b) after clustering image
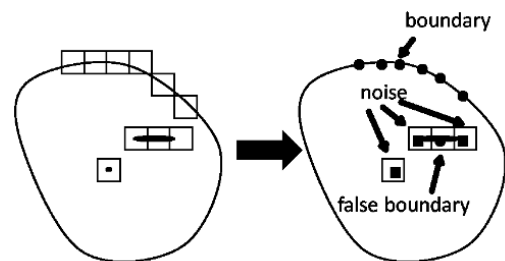
Fig. 5. Sparse PPA

3) Evaluate ∇f_e.
4) Boundary detection step:
    a) Set the boundary detection window.
    b) Apply SPPA boundary detection to ∇f_e with classifier $S_L(W,p)$ or $S_E(W,p)$.
    c) Enhance the gray level at p if it is classified as the boundary.
5) Noise removal step:
    a) Set the noise detection window.
    b) Smooth the entire window if the central point p of W is classified as the noise.
6) Evaluate new ∇f_e.
7) Run GGVF on the improved vector field.
8) Run the snake on the final vector field until convergence.

The algorithm seems to be similar to PPA-MRA, but actually it is not. As opposed to PPA-MRA the first step is the boundary detection combined with subsampling rather than the noise reduction. Secondly, the algorithm employs only one run. That is why it is fast and is easy to implement. Our forthcoming numerical experiments show that it works well with a variety of conventional filters and clustering

procedures and always contributes to the total accuracy increase.

IV. NUMERICAL RESULTS

Detection of tumors in the ultrasound images by a trained physician is usually efficient and the number of false negatives is low. However, manual segmentation of the tumor boundary is tedious and time-consuming. Therefore, automatic segmentation techniques are important to help us to better visualize the tumor boundary, to calculate the volume of the tumor and to extract features needed for the tumor classification (benign or malignant). This section presents experiments on real US images. The ground truth contours were outlined by Dr.Mavin Wongsaisuvan, who is currently a leading radiologist with the Queen Sirikit Center for Breast Cancer of King Chulalongkorn Memorial Hospital, Bangkok Thailand. The proposed GGVF-MRA-PPA and GGVF-SPPA are compared with GGVF and GGVF-MRA combined with the Gaussian smoothing (GS). The parameters of the algorithms are hand-tuned and the methods are compared when they perform the best (see similar evaluations in [77]). The parameters include the number of multiresolution levels and the size of the sampling windows. The accuracy is evaluated in terms of the percentage of the true positives and the average Hausdorff distance between the true contour and the snake given by

$$\text{dist}_H(C_T, C_S) =$$
$$\frac{\sum\limits_{a \in C_T} \min\limits_{b \in C_S} \frac{\|a-b\|}{N_T} + \sum\limits_{a \in C_S} \min\limits_{b \in C_T} \frac{\|a-b\|}{N_S}}{2}, \quad (10)$$

where N_T and N_S is the number of points belonging to the true contour and the snake respectively. In order to obtain a dimensionless estimate, the Hausdorff distance is divided by the length of the true contour L_{C_T}:

$$\text{dist}_{H,norm}(C_T, C_S) = \frac{\text{dist}_H(C_T, C_S)}{L_{C_T}}. \quad (11)$$

Measure (11) is a ratio of the Hausdorff distance between the snake and the true contour and the length of the true contour. For instance, the difference in 10 pixels is significant if the perimeter of the object is 100 pixels (a small object) but might not be that important if the length is 10000 pixels (a large object). Furthermore, the advantage of (10)-(11) is that it is a distance in a mathematical sense, whereas, the number of true positives is not. A combination of the true positives and the Hausdorff distance is a good measure of the segmentation quality. A larger degree of overlap of the boundaries (true positives) signifies a better segmentation. On the other hand, if the number of true positives is equal to zero, the boundaries could still be close, say at the distance of one pixel. In that case the Hausdorff distance shows that the quality of segmentation is still relatively good. In turn, a set of boundaries dissimilar only over small portions may have the same Hausdorff distance as that of the globally dissimilar set of boundaries. However, if the boundaries are globally dissimilar we may expect a very low number of true positives. Finally, if the number of true positives is high and the Hausdorff distance is low, the quality of segmentation is very likely to be good.

Our accuracy tables show the best accuracy from 100 GGVF iterations performed for $K = 0.01$ and $K = 0.1$. We also find the best preprocessing sequence for SPPA varying the filtering and the clustering methods. A bold font indicates the best result in the row and underlined bold is the best result for a particular initialization.

Example 1. Low contrast malignant tumor. Complicated shape.

The example of a tumor in Fig.6 shows the performance of a standard GGVF compared to GGVF-MRA-PPA and GGVF-FCM-SPPA. The snake has been initialized at an average Hausdorff distance of approximately 11, 17 and 22 pixels from the true boundary as follows. First, the snake is initialized inside a binary ground truth image which is "black" inside the tumor and "white" outside. Next, we let the snake grow until it reaches a certain distance from the boundary. Finally, we use this contour as the initial snake inside the real ultrasound image. The GGVF iterations are analyzed for extreme values of the diffusion coefficients: $K = 0.01$ (slow diffusion) and $K = 0.1$ (relatively high diffusion). Table 2 compares the performance of the proposed method with GGVF, GGVF-MRA and GGVF-MRA-GS in terms of the percentage of true positives, Hausdorff distance (10) and (11). Distance (11) is normalized as $\text{dist}_{H,norm}(C_T, C_S)10^3$ to avoid zeros after the decimal point.

We also include GGVF-MRA-PPA-D with discrete classifier (7) and continuous classifier (8). Note that the performance of exponential classifier (9) is practically the same as that of linear classifier (8). Therefore, we show only the PPA with classifier (8). The combination is denoted by GGVF-MRA-PPA-C. Next, we include GGVF-SPPA endowed with FCM. We also tested region growing(RG) [78], however the FCM on average works better. Finally, in order to enhance GGVF-SPPA we performed an exhaustive search considering different combinations of the filters: Gaussian filter(GS), median filter(MD), speckle filter(SP) as well as a morphological erosion/dilation routine(Morpho). Therefore, the 8th column of Table 2 shows the accuracy obtained with the best combination of methods whereas column 9th shows this combination. We denote this sequence of methods as "GGVF-SPPA+". Our exhaustive search for the mixture: "GGVF-SPPA+" is shown in Table 3. The tables show the accuracy for varying Hausdorff distance d between the initial snake and the true contour. The snakes are initialized at $d = 11, 17.4, 21.9$ and 27.8. Of course, the accuracy drops when d increases however the methods behave in a different way. The classical GGVF is unacceptable even when $d = 11$ (Table 2). The percentage of true positives is 59% and the average Hausdorff distance is almost 4 pixels from the true contour. It means that the resulting snake is very different from the ground truth. For this initialization all versions of GGVF-MRA generate about 90% accuracy and the Hausdorff distance of about 1.6. The use of PPA does not increase the accuracy. GGVF-FCM-SPPA produces 93% and 1.8 respectively: 3% increase of the true positives and 0.2 increase (not decrease) of the Hausdorff distance. However, as the initialization distance increases, the accuracy of all versions of GGVF-MRA drops faster than that of GGVF-FCM-SPPA. For instance, when $d = 27.8$ GGVF-MRA gives

only 55% true positive and 17 (!) pixel error. The PPA helps a lot, increasing the true positives to 85% and reducing the error to 2 pixels. However, this accuracy is still not sufficient. Surprisingly, GGVF-FCM-SPPA increases the accuracy to an acceptable 92% (1.8 pixels). Finally, GGVF-FCM-SPPA enhanced by the best preprocessing sequence shows 94% with a slight increase of the Hausdorff distance to 2 pixels. Clearly, for $d = 27.8$ the additional preprocessing does not make too much difference. Similar results are displayed for $d = 21.9$. However, for $d = 17.4$ the preprocessing works very well $94\% \rightarrow 98\%$ ($1.9 \rightarrow 1.5$). For this example the best preprocessing sequence is MD-SP-FCM-SPPA. Clearly, PPA and FCM-SPPA lead to a substantial accuracy increase for every initialization. However, the additional preprocessing shows a good performance only for small d. Finally, the conventional GGVF and GGVF-MRA are totally unacceptable for large d.

The resulting snakes corresponding to GGVF, GGFV-GS, GGVF-MRA, GGVF-MRA-PPA with classifiers (7) (8) and (9), GGVF-FCM-SPPA and GGVF-SPPA+ with the best preprocessing sequence are shown in Fig.6(c)-(g). For GGVF-MRA, the number of the multiresolution levels $N_L = 3$, $\Delta_1 = 0.81$, $\Delta_2 = 0.1$ and the window size $S_{max} = 15 \times 15$. The parameters of the classifier (7) are $\delta_{1,linear} = 0.25$, $\delta_{2,linear} = 0.86$. The boundary detection window of SPPA is $S_b = 5 \times 5$ and the noise detection window is $S_n = 13 \times 13$.

Recall that SPPA is much simpler and faster then MRA. That is why we analyze the ways to improve its efficiency combining with varying filtering and clustering image processing shown in Table 3. It shows the best combinations of preprocessing methods for each particular initialization of the snake as well as the relative impact of each component of the algorithm.

Example 2. Low contrast malignant tumor. Complicated structure of the noise. False boundary.

The image from Example 1 is characterized by an almost uniform background inside the tumor and a single large group of noise. This noise can be detected in one pass of GGVF-MRA when the sampling window becomes large enough. Consider an image in Fig.7. As opposed to Example 1 the noise is much more complicated. It includes several clusters scattered across the entire tumor. Some of the noise intensities are close to the intensities of pixels nearby the boundary. Such structures are hard to classify and eliminate. Besides, the tumor is characterized by a false boundary at the right side of the image(Fig.7(a)).

The testing results are organized similarly to Example 1.

Table 4 demonstrates that with these image features the segmentation is intractable for conventional GGVF (Fig.7(c)). However, GGVF enhanced by MRA and subjected to a GS works much better. Again the methods behave in a different way. For instance, consider the conventional GGVF. The accuracy of about 65% is low even when $d = 6.8$ although the Hausdorff distance 3.2 pixels seems to be relatively small. However, GGVF-MRA-PPA-D, GGVF-MRA-PPA-C, GGVF-FCM-SPPA, GGVF-SPPA+ produce the accuracy of 95% and higher. Even when the distance is about 21 pixels GGVF-MRA-PPA-C and GGVF-MRA-PPA-D generate a 96% accurate segmentation whereas the
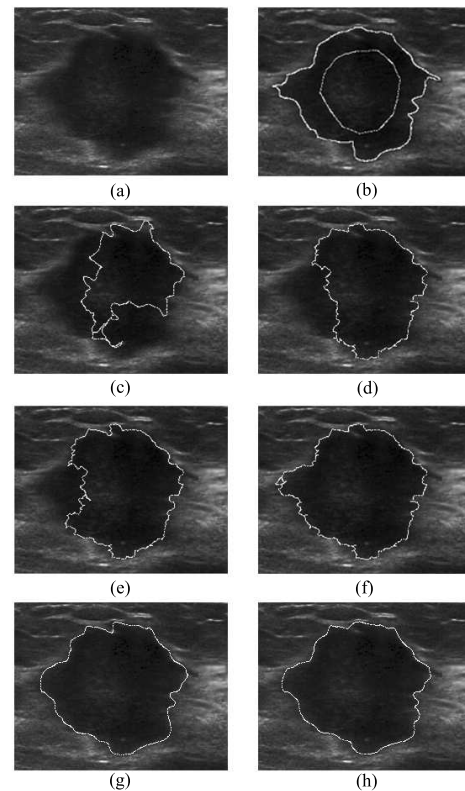
Fig. 6. Example 1. Low contrast US image, (782×616), ($d = 22$). (a) The original image, (b) the initial contour and the ground truth, (c) GGVF, (d) GGVF-MRA, (e) GGVF-MRA-GS, (f) GGVF-MRA-PPA, (g) GGVF-FCM-SPPA, (h) GGVF-SPPA+.
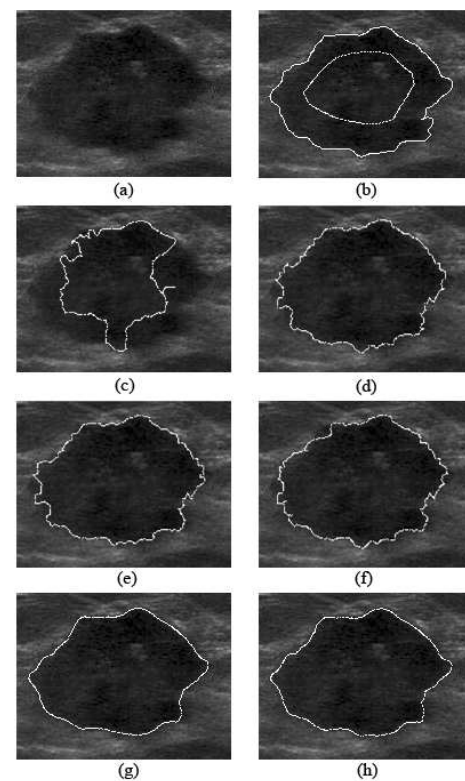
Fig. 7. Example 2. Low contrast US image, (687×535), ($d = 21$). (a) The original image, (b) the initial contour and the ground truth, (c) GGVF, (d) GGVF-MRA, (e) GGVF-MRA-GS, (f) GGVF-MRA-PPA, (g) GGVF-FCM-SPPA, (h) GGVF-SPPA+.
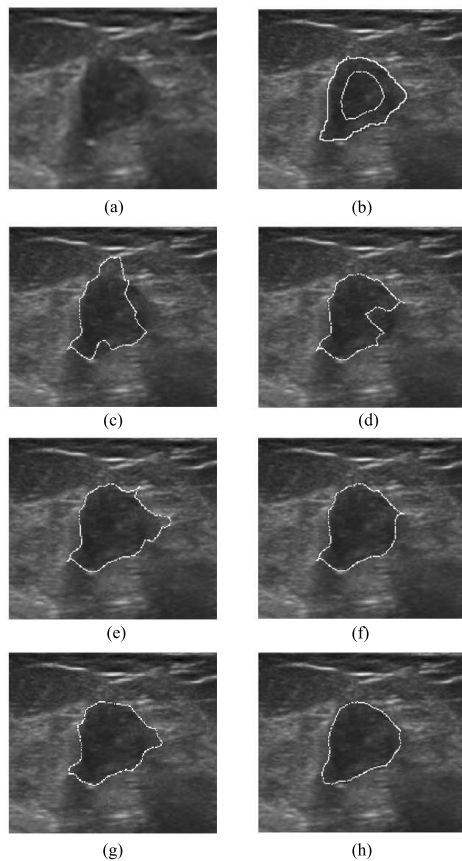
Fig. 8. Example 3. Low contrast US image, (500×434), $(d = 12.2)$. (a) The original image, (b) the initial contour and the ground truth, (c) GGVF, (d) GGVF-MRA, (e) GGVF-MRA-GS, (f) GGVF-MRA-PPA, (g) GGVF-FCM-SPPA, (h) GGVF-SPPA+.

accuracy of GGVF is totally unacceptable (see Fig.7). Note that SPPA shows a slightly lower accuracy in terms of true positives: 94% as well as in terms of the Hausdorff distance: 1.274 vs. 1.251. However, for $d = 9.1$ SPPA performance is almost the same as for $d = 12.6$ and even slightly better(96.8 vs. 95.8).

Consider Table 5. The table shows how to improve the efficiency of SPPA with regard to GGVF combined with different filtering and clustering. The GGVF combined with the GS and MD generates good results for $d = 6.8$, $d = 9.1$ and $d = 12.6$ comparable with and even slightly better than SPPA. However, for $d = 20.9$ the accuracy of GGVF drops drastically : 76%. However, SPPA-FCM still leads to an excellent 94%.

For this experiment, the number of the multiresolution levels $N_L = 3$, $\Delta_1 = 0.85$, $\Delta_2 = 0.1$ and the window size $S_{max} = 10 \times 10$. The parameters of classifier (7) are $\delta_{1,linear} = 0.25$, $\delta_{2,linear} = 0.825$. The boundary detection window of SPPA is $S_b = 5 \times 5$ and the noise detection window is $S_n = 13 \times 13$.

Example 3. Low contrast benign tumor. High level of noise.

It is plain that the noise inside the tumor in Fig. 8 is high. Moreover, the boundary is not clearly defined. However, an experienced radiologist is often able to hand-drawn the boundary with a high precision. When we asked several

radiologists to draw the same tumor, the results were different but not more than 3-4% in terms of the Hausdorff distance. Let us compare now the accuracy of the radiologist and our proposed segmentation routines. The testing results are organized similarly to Examples 1 and 2 in Tables 6 and 7. The snakes are initialized at $d = 8.7$, 10.8, 12.2 and 13.9. The largest distance 13.9 is smaller than in Examples 1 and 2 because the tumor is smaller as well. However, the ratio $\frac{Area}{2\pi \max(d)}$ is approximately the same for all tumors.

Furthermore, GGVF-FCM-SPPA performs similarly to all the versions of GGVF-MRA. However, the performance is poor, not exceeding 89%. The accuracy practically does not depend on the initialization due to a high level of noise everywhere inside the tumor. However, GGVF-SPPA with an appropriate preprocessing leads to a 98% accuracy (!). Note that 98% is actually higher than we need since the accuracy of the radiologists does not exceed 97%. The best preprocessing sequences are GS-MD-FCM-SPPA (3 times) and MD-FCM-SPPA (1 time) whereas Morpho, SP and RG do not achieve good results.

For this experiment, the number of the multiresolution levels $N_L = 2$, $\Delta_1 = 0.8$, $\Delta_2 = 0.1$ and the window size $S_{max} = 3 \times 3$. The parameters of classifier (7) are $\delta_{1,linear} = 0.25$, $\delta_{2,linear} = 0.7$. The boundary detection window of SPPA is $S_b = 2 \times 2$ and the noise detection window is $S_n = 5 \times 5$.

V. CONCLUSION

The proposed combinations GGVF-MRA-PPA and GGVF-FCM-SPPA applied to segmentation of the US tumor images of the breast are capable of increasing the accuracy of the segmentation up to 30% in terms of true positives and in 2-3 times in terms of Hausdorff distance between the true boundary and the resulting snake. GGVF-FCM-SPPA is easier to implement and faster, however its efficiency is often comparable with GGVF-MRA-PPA. The methods show promising results when applied to the initial contour positioned far from the true boundary. Due to its local nature, the methods work very well with the noise represented by a large group of pixels with the intensity different from the local background. The numerical experiments make it possible to conjecture that the proposed techniques will succeed in segmentation of a variety of tumors displayed in ultrasound images of the breast.

TABLE II
EXAMPLE 1. THE BEST ACCURACY(PERCENTAGE OF TRUE POSITIVES AND THE HAUSDORFF DISTANCE OF GGVF, GGVF-MRA, GGVF-MRA-GS, GGVF-MRA-PPA-D, GGVF-MRA-PPA-C, GGVF-FCM-SPPA, AND GGVF-SPPA+) VS. THE DISTANCE BETWEEN THE INITIAL CONTOUR AND THE TRUE BOUNDARY.

d (pixels)	GGVF	GGVF-MRA	GGVF-MRA -GS	GGVF-MRA -PPA-D	GGVF-MRA -PPA-C	GGVF-FCM -SPPA	GGVF-SPPA+	PP
11.0	59.085	90.530	90.688	90.917	90.741	93.836	98.154	MD-SP
	3.755	1.624	1.142	1.683	1.694	1.853	1.554	-FCM-PPA
	4.994	2.160	2.828	2.238	2.252	2.465	2.066	
17.4	42.154	89.715	87.132	91.605	91.321	94.542	98.801	MD-SP
	6.975	1.657	1.742	1.661	1.688	1.952	1.599	-FCM-PPA
	9.275	2.204	2.316	2.209	2.244	2.595	2.126	
21.9	29.930	72.873	71.965	91.760	91.573	92.020	95.504	MD-SP
	18.289	8.237	6.600	1.694	1.709	1.915	2.201	-FCM-PPA
	24.230	10.953	8.777	2.253	2.272	2.547	2.926	
27.8	15.281	62.075	55.636	85.632	84.571	92.833	94.231	MD-GS
	23.215	9.205	17.940	2.280	2.293	1.895	2.581	-FCM-SPPA
	30.872	12.240	23.857	3.031	3.049	2.520	3.432	

TABLE III
EXAMPLE 1. THE ACCURACY OBTAINED WITH THE DIFFERENT COMBINATION OF FILTERS MEASURED BY TRUE POSITIVES AND THE HAUSDORFF DISTANCE.

d	Filter	GGVF			GGVF-FCM			GGVF-FCM-SPPA			GGVF-RG			GGVF-RG-SPPA		
11.0	GS	62.986	4.640	6.170	88.976	2.058	2.736	91.696	1.948	2.591	81.951	2.494	3.316	94.078	1.896	2.522
	MD	65.264	4.435	5.898	90.969	2.149	2.857	91.172	2.072	2.756	84.341	2.440	3.245	**96.181**	**1.842**	**2.450**
	SP	52.305	5.957	7.922	88.262	2.107	2.802	87.294	2.294	3.051	80.028	2.523	3.355	86.603	2.171	2.887
	Morpho	45.859	6.954	9.248	85.559	2.290	3.045	85.647	2.277	3.027	75.562	2.828	3.761	82.923	2.394	3.184
	GS-SP	59.567	5.303	7.052	88.732	2.079	2.765	92.164	1.923	2.557	76.130	2.782	3.699	78.779	2.591	2.446
	GS-MD	68.475	4.173	5.550	88.480	2.125	2.826	91.993	1.968	2.617	83.703	2.434	3.237	90.065	2.014	2.678
	MD-SP	66.946	4.274	5.683	**97.529**	**1.579**	**2.100**	**98.154**	**1.554**	**2.066**	85.007	2.404	3.196	87.680	2.063	2.744
	MD-GS	**70.957**	**4.025**	**5.352**	94.581	1.772	2.356	93.954	1.819	2.420	81.193	2.506	3.332	77.500	2.665	3.544
	SP-GS	64.409	4.537	6.033	88.424	2.109	2.805	92.308	1.925	2.559	73.729	2.995	3.982	75.458	3.074	4.087
	SP-MD	64.441	4.649	6.183	95.214	1.690	2.247	96.075	1.620	2.155	72.929	3.098	4.119	78.628	2.740	3.644
17.4	GS	68.411	4.606	6.125	88.399	2.096	2.788	94.903	1.897	2.523	79.513	2.776	3.692	93.939	1.897	2.522
	MD	70.019	4.439	5.903	91.167	2.108	2.803	95.946	1.850	2.460	83.776	2.564	3.410	**96.454**	**1.841**	**2.448**
	SP	62.549	5.086	6.763	87.786	2.125	2.826	87.102	2.223	2.956	72.077	3.184	4.234	87.317	2.138	2.844
	Morpho	46.104	7.344	9.766	85.498	2.290	3.045	85.647	2.277	3.027	75.493	2.928	3.893	83.146	2.349	3.123
	GS-SP	67.573	4.604	6.122	88.854	2.076	2.761	94.107	1.912	2.542	75.294	2.922	3.886	82.226	2.417	3.214
	GS-MD	**77.756**	**4.093**	**5.442**	89.338	2.070	2.752	94.983	1.932	2.570	81.308	2.591	3.445	90.186	1.980	2.633
	MD-SP	73.281	4.235	5.632	**97.256**	**1.599**	**2.126**	**98.801**	**1.599**	**2.126**	84.202	2.424	3.223	88.255	2.059	2.738
	MD-GS	75.425	4.115	5.473	94.454	1.786	2.375	97.124	1.711	2.275	81.269	2.535	3.372	80.261	2.477	3.294
	SP-GS	70.019	4.538	6.035	88.748	2.078	2.763	94.681	1.932	2.570	72.793	3.155	4.195	77.331	2.896	3.850
	SP-MD	76.181	4.181	5.559	95.353	1.697	2.257	98.039	1.638	2.238	71.259	3.243	4.313	78.369	2.779	3.696
21.9	GS	57.884	10.959	14.573	71.717	8.302	11.040	92.190	1.930	2.567	59.076	9.012	11.984	93.976	1.893	2.517
	MD	59.394	9.939	13.217	72.414	8.558	11.380	92.639	2.430	3.232	69.335	7.444	9.899	**95.014**	**1.851**	**2.462**
	SP	54.237	11.080	14.734	70.420	8.812	11.718	90.236	2.065	2.746	47.310	11.613	15.442	85.331	2.371	3.152
	Morpho	25.000	17.540	23.325	68.719	8.830	11.742	86.505	2.951	3.924	56.574	10.893	14.486	80.746	2.533	3.368
	GS-SP	60.041	10.125	13.465	71.499	8.176	10.872	91.176	2.597	3.454	63.361	5.251	6.983	76.151	2.778	3.694
	GS-MD	**67.360**	**9.076**	**12.070**	71.144	7.772	10.335	91.155	2.620	3.484	68.170	4.750	6.316	90.718	1.957	2.603
	MD-SP	63.445	9.935	13.211	**79.268**	**8.130**	**10.811**	95.504	2.201	2.926	70.082	4.693	6.241	89.713	1.984	2.639
	MD-GS	64.777	9.678	12.869	77.381	7.907	10.514	94.946	2.255	2.999	**79.173**	**2.813**	**3.741**	83.250	2.423	3.222
	SP-GS	59.192	10.491	13.951	71.901	8.170	10.864	91.160	2.653	3.529	70.275	4.259	5.663	80.127	2.661	3.539
	SP-MD	65.451	9.544	12.691	75.315	8.248	10.969	93.659	2.438	3.242	68.412	4.245	5.645	80.467	2.693	3.581
27.8	GS	27.696	21.354	28.396	55.668	12.755	16.961	92.542	1.851	2.462	46.886	18.970	25.226	73.485	3.251	4.323
	MD	43.840	17.707	23.546	68.716	9.297	12.363	90.982	2.791	3.712	60.530	11.038	14.679	**92.945**	**1.995**	**2.653**
	SP	23.757	23.318	31.008	55.779	12.837	17.071	91.751	1.955	2.599	44.533	20.740	27.580	79.909	3.003	3.993
	Morpho	8.150	30.431	40.466	51.939	13.217	17.575	83.799	3.468	4.611	45.611	19.986	26.577	79.456	2.751	3.658
	GS-SP	42.197	18.417	24.491	57.468	12.358	16.433	86.139	3.313	4.401	54.064	10.715	14.248	77.344	2.840	3.777
	GS-MD	44.828	12.768	16.979	72.122	8.759	11.647	90.438	2.864	3.809	62.153	9.173	12.198	90.385	1.964	2.612
	MD-SP	**45.892**	**17.755**	**23.611**	61.111	12.433	16.534	93.191	2.534	3.369	65.033	9.165	12.187	89.601	1.986	2.641
	MD-GS	37.607	16.626	22.109	**76.354**	**8.620**	**11.462**	94.231	2.581	3.432	**78.989**	**2.882**	**3.832**	81.877	2.520	3.351
	SP-GS	38.827	19.363	25.748	56.788	12.521	16.650	87.879	2.113	2.810	51.453	11.100	14.761	78.022	2.789	3.708
	SP-MD	42.204	14.963	19.897	75.240	8.816	11.723	92.916	1.798	2.392	68.151	4.353	5.786	80.308	2.701	3.592

TABLE IV
EXAMPLE 2. THE BEST ACCURACY VS. THE DISTANCE BETWEEN THE INITIAL CONTOUR AND THE TRUE BOUNDARY.

d (pixels)	GGVF	GGVF-MRA	GGVF-MRA-GS	GGVF-MRA-PPA-D	GGVF-MRA-PPA-C	GGVF-FCM-SPPA	GGVF-SPPA+	PP
6.8	65.605	85.259	83.960	95.592	95.338	95.697	96.916	GS-MD
	3.200	1.791	1.903	1.499	1.506	1.051	1.183	
	10.988	3.459	3.506	3.392	3.407	2.378	2.677	
9.1	56.899	83.534	83.951	96.110	96.279	96.008	96.721	GS-FCM-SPPA
	3.998	1.956	2.012	1.510	1.523	1.047	1.042	
	9.103	3.468	3.517	3.416	3.446	2.368	2.357	
12.6	22.179	75.960	77.688	94.989	96.136	96.074	96.835	GS-FCM-SPPA
	11.672	2.923	2.681	1.534	1.488	1.048	1.037	
	27.159	4.505	4.306	3.368	3.366	2.371	2.345	
20.9	16.763	67.561	68.245	96.625	96.625	93.966	94.297	MD-GS-FCM-SPPA
	18.795	5.006	6.253	1.251	1.251	1.385	1.274	
	42.523	11.325	14.148	2.829	2.829	3.134	2.882	

TABLE V
EXAMPLE 2. THE ACCURACY OBTAINED WITH THE DIFFERENT COMBINATION OF FILTERS MEASURED BY TRUE POSITIVES AND THE HAUSDORFF DISTANCE.

d	Filter	GGVF			GGVF-FCM			GGVF-FCM-SPPA			GGVF-RG			GGVF-RG-SPPA		
6.8	GS	96.610	1.011	2.287	**96.368**	**1.035**	**2.343**	95.378	1.055	2.387	84.270	1.459	3.300	82.705	1.529	3.60
	MD	90.719	1.529	2.459	93.946	1.190	2.693	94.004	1.189	2.689	83.028	1.515	3.427	83.556	1.563	3.535
	SP	85.957	2.167	4.903	93.763	1.243	2.812	92.813	1.278	2.892	80.920	1.934	4.375	84.018	1.4872	3.363
	Morpho	91.519	1.388	3.140	94.726	1.359	3.074	90.675	1.520	3.439	76.644	2.472	5.594	88.608	1.550	3.507
	GS-SP	91.379	1.367	3.093	92.946	1.430	3.236	84.736	1.995	4.514	88.194	1.390	3.146	87.838	1.409	3.188
	GS-MD	**96.916**	**1.183**	**2.677**	92.888	1.379	3.121	84.493	1.956	4.425	**93.556**	**1.175**	**2.658**	**94.967**	**1.162**	**2.628**
	MD-SP	73.307	2.998	6.783	92.903	1.395	3.157	80.961	2.230	5.046	85.349	1.398	3.162	84.305	1.435	3.247
	MD-GS	88.866	1.724	3.901	94.130	1.257	2.844	85.150	1.835	4.153	90.654	1.279	2.894	90.508	1.285	2.907
	SP-GS	96.320	1.005	2.273	93.750	1.357	3.071	82.975	1.972	4.462	82.232	1.598	3.615	81.316	1.658	3.752
	SP-MD	86.263	1.853	4.192	93.043	1.325	2.997	80.843	2.651	5.998	93.079	1.151	2.604	93.435	1.131	2.560
9.1	GS	94.770	1.243	2.811	**93.978**	**1.389**	**3.142**	**96.721**	**1.042**	**2.357**	85.874	1.411	3.192	82.965	1.510	3.417
	MD	92.934	1.549	3.504	93.548	1.265	2.861	93.418	1.191	2.695	83.222	1.500	3.395	82.529	1.602	3.625
	SP	86.364	2.155	4.875	92.017	1.501	3.396	93.320	1.271	2.876	67.679	2.794	6.321	80.899	1.695	3.835
	Morpho	92.292	1.482	3.353	92.355	1.608	3.637	90.138	1.530	3.461	67.292	3.157	7.143	89.831	1.559	3.526
	GS-SP	90.987	1.492	3.375	92.693	1.515	3.427	85.516	1.961	4.437	87.788	1.394	3.155	86.712	1.456	3.293
	GS-MD	**96.484**	**1.204**	**2.724**	92.391	1.409	3.187	84.008	1.973	4.465	**92.019**	**1.246**	**2.819**	**94.647**	**1.148**	**2.598**
	MD-SP	75.306	2.814	6.367	93.206	1.383	3.130	83.460	1.919	4.341	83.447	1.490	3.372	84.807	1.414	3.199
	MD-GS	88.161	1.790	4.051	93.474	1.301	2.944	85.526	1.831	4.141	84.036	1.796	4.063	90.044	1.302	2.945
	SP-GS	94.553	1.226	2.773	92.276	1.566	3.542	84.191	1.825	4.128	84.685	1.510	3.416	81.585	1.661	3.758
	SP-MD	85.830	1.958	4.431	92.609	1.367	3.093	81.445	2.567	5.808	86.605	1.698	3.842	93.833	1.141	2.582
12.6	GS	95.415	1.315	2.976	86.410	2.033	4.599	**96.835**	**1.037**	**2.345**	83.990	1.553	3.513	82.639	1.514	3.426
	MD	91.574	1.633	3.694	92.088	1.424	3.222	93.617	1.198	2.710	75.829	2.084	4.714	82.339	1.564	3.539
	SP	86.422	2.167	4.903	91.579	1.575	3.563	94.068	1.247	2.820	62.585	3.287	7.437	80.272	1.708	3.863
	Morpho	84.411	2.132	4.823	92.000	1.667	3.772	90.533	1.525	3.450	61.573	3.594	8.131	78.054	2.352	5.321
	GS-SP	93.348	1.450	3.281	90.756	1.641	3.713	93.568	1.440	3.258	82.108	1.972	4.461	86.927	1.446	3.272
	GS-MD	**95.815**	**1.235**	**2.795**	92.291	1.472	3.329	84.942	1.898	4.294	**85.856**	**1.868**	**4.227**	**94.570**	**1.168**	**2.643**
	MD-SP	80.477	2.279	5.155	**92.489**	**1.407**	**3.184**	87.791	1.655	3.744	79.075	2.024	4.579	82.135	1.575	3.564
	MD-GS	88.503	1.698	3.841	92.421	1.455	3.292	84.310	1.859	4.207	83.960	1.874	4.241	88.210	1.434	3.244
	SP-GS	95.506	1.274	2.883	92.191	1.642	3.715	94.055	1.366	3.090	83.750	1.552	3.512	80.795	1.656	3.747
	SP-MD	88.683	1.752	3.964	91.868	1.451	3.282	88.086	1.569	3.550	84.887	1.825	4.130	93.640	1.157	2.617
20.9	GS	45.688	10.364	23.449	37.975	9.691	21.924	94.255	1.386	3.135	77.096	1.902	4.304	83.683	1.509	3.414
	MD	75.402	3.457	7.821	70.172	3.567	8.070	94.280	1.191	2.694	77.917	1.855	4.198	82.477	1.529	3.458
	SP	24.190	13.429	30.381	63.158	4.883	11.048	94.215	1.261	2.852	61.552	3.236	7.321	87.050	1.400	3.169
	Morpho	32.648	10.772	24.371	48.519	8.607	19.474	94.191	1.394	3.153	67.816	3.126	7.072	78.242	2.220	5.024
	GS-SP	72.315	3.437	7.775	68.352	3.930	8.892	93.125	1.453	3.287	79.626	1.847	4.178	88.263	1.394	3.154
	GS-MD	**76.402**	**3.158**	**7.146**	73.733	3.227	7.300	93.082	1.425	3.224	**89.732**	**1.362**	**3.081**	89.401	1.353	3.060
	MD-SP	73.672	3.141	7.107	**75.000**	**3.099**	**7.010**	93.004	1.384	3.130	80.342	1.725	3.904	81.818	1.584	3.585
	MD-GS	76.112	3.239	7.329	74.023	3.155	7.139	**94.297**	**1.274**	**2.882**	82.563	1.956	4.426	**89.786**	**1.293**	**2.925**
	SP-GS	58.219	5.146	11.644	68.615	4.060	9.185	93.750	1.363	3.084	77.895	1.722	3.897	82.270	1.597	3.614
	SP-MD	76.152	3.187	7.211	70.404	3.529	7.984	93.697	1.361	3.079	84.479	1.829	4.138	93.267	1.143	2.587

TABLE VI
EXAMPLE 3. THE BEST ACCURACY VS. THE DISTANCE BETWEEN THE INITIAL CONTOUR AND THE TRUE BOUNDARY.

d (pixels)	GGVF	GGVF-MRA	GGVF-MRA-GS	GGVF-MRA-PPA-D	GGVF-MRA-PPA-C	GGVF-FCM-SPPA	GGVF-SPPA+	PP
8.7	71.482	81.915	82.105	86.561	87.925	88.028	98.406	GS-MD-FCM-SPPA
	3.126	2.144	2.125	1.825	1.709	1.949	1.470	
	8.416	6.993	6.915	5.965	5.585	6.370	4.805	
10.8	68.932	82.230	81.915	89.558	88.302	88.489	98.785	MD-FCM-SPPA
	2.797	2.140	2.147	1.797	1.758	1.948	1.384	
	10.007	6.847	7.022	5.874	5.762	6.365	4.524	
12.2	55.670	71.000	74.593	87.059	87.833	89.085	98.374	GS-MD-FCM-SPPA
	4.735	3.435	2.276	1.825	1.774	1.952	1.476	
	12.958	8.530	7.508	5.954	5.796	6.380	4.824	
13.9	47.745	68.354	71.238	89.558	88.302	89.209	98.795	GS-MD-FCM-SPPA
	5.309	2.501	3.480	1.797	1.758	1.931	1.451	
	15.017	9.636	8.446	5.846	5.746	6.311	4.740	

TABLE VII
EXAMPLE 3. THE ACCURACY OBTAINED WITH THE DIFFERENT COMBINATION OF FILTERS MEASURED BY TRUE POSITIVES AND THE HAUSDORFF DISTANCE.

d	Filter	GGVF			GGVF-FCM			GGVF-FCM-SPPA			GGVF-RG			GGVF-RG-SPPA		
8.7	GS	85.232	2.042	6.673	**95.000**	**1.926**	**6.295**	98.155	1.554	5.080	63.462	4.072	13.306	**91.532**	**1.718**	**5.613**
	MD	84.255	2.107	6.886	89.496	1.850	6.047	98.381	1.387	4.534	63.348	3.663	11.970	81.328	2.615	8.546
	SP	76.400	2.563	8.377	93.227	1.872	6.117	93.750	1.649	5.390	70.984	3.880	12.679	88.259	1.681	5.499
	Morpho	75.847	2.348	7.672	84.644	2.187	7.149	88.448	1.890	6.177	68.372	3.201	10.459	89.641	1.594	5.209
	GS-SP	82.645	2.263	7.395	90.400	2.011	6.571	97.328	1.626	5.315	58.289	4.895	15.995	73.478	3.112	10.171
	GS-MD	88.983	1.773	5.795	90.871	1.855	6.063	**98.406**	**1.470**	**4.805**	60.086	3.984	13.020	79.693	2.702	8.830
	MD-SP	90.558	1.731	5.656	79.752	2.395	7.828	95.868	1.752	5.725	55.049	5.049	16.501	71.064	3.091	10.102
	MD-GS	**93.913**	**1.471**	**4.808**	88.259	2.097	6.853	96.850	1.677	5.482	58.108	3.935	12.858	85.081	2.507	8.194
	SP-GS	88.115	1.868	6.105	90.076	2.055	6.717	96.958	1.592	5.203	67.980	3.820	12.484	79.268	3.080	10.066
	SP-MD	92.116	1.594	5.209	90.574	1.859	6.074	98.367	1.426	4.662	**71.362**	**3.445**	**11.258**	81.061	2.418	7.902
10.8	GS	90.045	2.097	6.852	**92.672**	**2.172**	**7.098**	98.485	1.533	5.011	58.108	5.012	16.378	**91.600**	**1.723**	**5.631**
	MD	83.722	2.046	6.685	86.842	2.168	7.085	**98.785**	**1.384**	**4.524**	65.899	3.714	12.137	80.498	2.672	8.733
	SP	82.251	2.367	7.734	90.295	2.197	7.179	94.526	1.627	5.318	58.605	4.976	16.262	81.513	2.421	7.912
	Morpho	72.247	2.750	8.987	81.673	2.500	8.171	91.228	1.840	6.012	**75.122**	**3.222**	**10.528**	86.770	1.696	5.544
	GS-SP	84.979	2.188	7.150	85.944	2.310	7.548	96.565	1.621	5.297	52.151	5.205	17.111	74.561	3.096	10.117
	GS-MD	91.111	1.778	5.810	87.826	2.105	6.878	98.381	1.471	4.408	62.617	4.007	13.096	78.519	2.727	8.911
	MD-SP	92.478	1.891	6.181	75.771	2.786	9.106	94.958	1.730	5.654	57.692	5.137	16.786	72.650	3.070	10.033
	MD-GS	92.342	1.750	5.720	85.124	2.328	7.608	96.429	1.676	5.477	53.879	5.046	16.492	84.362	2.541	8.305
	SP-GS	87.124	2.099	6.858	87.295	2.308	7.542	97.710	1.597	5.218	69.652	3.902	12.750	79.668	3.087	10.088
	SP-MD	**93.151**	**1.722**	**5.792**	86.307	2.153	7.037	97.967	1.427	4.664	70.952	3.577	11.690	79.151	2.440	7.973
12.2	GS	88.584	2.207	7.211	**90.308**	**2.303**	**7.527**	97.810	1.551	5.068	57.576	5.245	17.142	**92.713**	**1.717**	**5.610**
	MD	84.793	2.154	7.040	84.375	2.225	7.272	98.000	1.399	4.571	56.223	5.086	16.620	82.231	2.608	8.523
	SP	82.727	2.381	7.782	85.957	2.366	7.734	94.340	1.612	5.269	49.565	5.921	19.349	80.176	2.645	8.645
	Morpho	69.507	2.966	9.693	78.205	2.618	8.555	88.968	1.875	6.126	**74.762**	**3.240**	**10.587**	86.434	1.686	5.509
	GS-SP	83.186	2.265	7.401	84.716	2.390	7.811	97.701	1.618	5.289	32.813	8.665	28.317	73.799	3.117	10.186
	GS-MD	88.646	1.907	6.231	87.168	2.185	7.142	**98.374**	**1.476**	**4.824**	55.046	5.359	17.512	78.277	2.725	8.905
	MD-SP	**90.868**	**1.985**	**6.485**	73.077	3.010	9.837	94.239	1.764	5.764	41.935	6.735	22.011	72.414	3.088	10.092
	MD-GS	87.168	1.926	6.294	82.589	2.445	7.991	96.016	1.687	5.513	54.505	5.291	17.290	83.871	2.549	8.332
	SP-GS	85.520	2.198	7.182	86.266	2.407	7.867	97.761	1.591	5.200	62.439	5.140	16.798	79.583	3.082	10.071
	SP-MD	88.889	1.933	6.316	84.821	2.291	7.486	98.016	1.423	4.652	59.912	4.930	16.112	78.113	2.451	8.009
13.9	GS	88.739	2.164	7.071	**90.000**	**2.209**	**7.220**	98.524	1.543	5.044	38.333	9.199	30.063	**83.539**	**2.731**	**8.923**
	MD	88.995	2.042	6.675	85.909	2.173	7.102	98.419	1.369	4.475	55.172	5.626	18.387	79.508	2.783	9.094
	SP	87.330	2.127	6.950	89.778	2.223	7.264	93.548	1.651	5.395	28.708	10.468	34.209	79.646	2.621	8.564
	Morpho	66.810	3.185	10.410	81.857	2.531	8.272	88.612	1.872	6.118	**72.000**	**3.325**	**10.865**	79.487	2.770	9.051
	GS-SP	86.385	2.256	7.373	87.719	2.286	7.472	97.368	1.620	5.295	18.966	10.910	35.652	74.026	3.108	10.155
	GS-MD	**92.056**	**1.944**	**6.352**	87.273	2.159	7.055	**98.810**	**1.443**	**4.715**	41.969	8.110	26.503	78.491	2.714	8.871
	MD-SP	90.698	2.052	6.705	71.861	2.988	9.765	94.606	1.760	5.571	21.429	12.284	40.145	71.795	3.091	10.102
	MD-GS	88.000	2.025	6.617	83.408	2.378	7.772	95.547	1.683	5.499	40.957	7.960	26.012	83.182	2.539	8.297
	SP-GS	86.818	2.235	7.303	87.446	2.314	7.562	97.794	1.609	5.257	40.107	7.891	25.789	80.426	3.053	9.976
	SP-MD	91.905	1.970	6.437	86.239	2.173	7.102	97.942	1.431	4.678	48.756	6.020	19.673	79.608	2.445	7.990

(Advance online publication: 25 May 2011)

References

[1] M. Kass, A. Witkin, and D. Terzopoulos, "Snakes: Active contour models," *International Journal of Computer Vision*, vol. 1, no. 4, pp. 321–331, 1988.

[2] D. Kuan, A. Sawchuk, T. Strand, and P. Chavel, "Adaptive restoration of images with speckle," *IEEE Transactions on Acoustics Speech and Signal Processing*, vol. 35, no. 3, pp. 373–383, 1987.

[3] A. Evans and M. Nixon, "Biased motion-adaptive temporal filtering for speckle reduction in echocardiography," *IEEE Transactions on Medical Imaging*, vol. 15, no. 1, pp. 39–50, 1996.

[4] F. Lefebvre, G. Berger, and P. Laugier, "Automatic detection of the boundary of the calcaneus from ultrasound parametric images using an active contour model: Clinical assessment," *IEEE Trans. Med. Imaging*, vol. 17, no. 1, pp. 45–52, 1998.

[5] Y. S. Akgul, C. Kambhamettu, and M. Stone, "Extraction and tracking of the tongue surface from ultrasound image sequences," in *Proceedings of the IEEE Computer Society Conference on Computer Vision and Pattern Recognition*, ser. CVPR '98. Washington, DC, USA: IEEE Computer Society, 1998, pp. 298–303.

[6] R. Chung and K.-K. Ho, "Using 2d active contour models for 3d reconstruction from serial sections," in *Proceedings of the 1996 International Conference on Pattern Recognition (ICPR '96) Volume I - Volume 7270*, 1996, pp. 849–853.

[7] A. Fenster, S. Tong, H. Cardinal, C. Blake, and D. Downey, "Three-dimensional ultrasound imaging system for prostate cancer diagnosis and treatment," *Instrumentation and Measurement, IEEE Transactions on*, vol. 47, no. 6, pp. 1439 –1447, 1998.

[8] M. Strintzis and I. Kokkinidis, "Maximum likelihood motion estimation in ultrasound image sequences," *Signal Processing Letters, IEEE*, vol. 4, no. 6, pp. 156 –157, 1997.

[9] D. Chen, R. Chang, W. Wu, W. Moon, and W. Wu, "3-d breast ultrasound segmentation using active contour model," *Ultrasound in Med. and Biology*, vol. 29, no. 7, pp. 1017–1026, 2003.

[10] R.-F. Chang, W.-J. Wu, W. K. Moon, W.-M. Chen, W. Lee, and D.-R. Chen, "Segmentation of breast tumor in three-dimensional ultrasound images using three-dimensional discrete active contour model," *Ultrasound in Medicine & Biology*, vol. 29, no. 11, pp. 1571–1581, 2003.

[11] M. Cvancarova, F. Albresgtsen, K. Brabrand, and E. Samset, "Segmentation of ultrasound images of liver tumors applying snake algorithms and gvf," *Congress Series*, vol. 1281, pp. 218–223, 2005.

[12] M. Aleman-Flores, P. Aleman-Flores, L. Alvarez-Leon, M. Esteban-Sanchez, R. Fuentes-Pavon, and J. Santana-Montesdeoca, "Computerized ultrasound characterization of breast tumors," *International Congress Series*, vol. 1281, pp. 1063 – 1068, 2005.

[13] L. D. Cohen, "On active contour models and balloons," *Computer Vision, Graphics, and Image Processing. Image Understanding*, vol. 53, no. 2, pp. 211–218, 1991.

[14] L. D. Cohen and I. Cohen, "Finite element methods for active contour models and balloons for 2d and 3d images," *IEEE Transactions on Pattern Analysis and Machine Intelligence*, vol. 15, pp. 1131–1147, 1991.

[15] O. Pujol, D. Gil, and P. Radeva, "Fundamentals of stop and go active models," *Image Vision Comput.*, vol. 23, pp. 681–691, 2005.

[16] J. Tang, "A multi-direction gvf snake for the segmentation of skin cancer images," *Pattern Recogn.*, vol. 42, pp. 1172–1179, 2009.

[17] F. Y. Shih and K. Zhang, "Locating object contours in complex background using improved snakes," *Comput. Vis. Image Underst.*, vol. 105, pp. 93–98, 2007.

[18] I. Dagher and K. E. Tom, "Waterballoons: A hybrid watershed balloon snake segmentation," *Image Vision Comput.*, vol. 26, pp. 905–912, 2008.

[19] X. Zhu, P. Zhang, J. Shao, Y. Cheng, Y. Zhang, and J. Bai, "A snake-based method for segmentation of intravascular ultrasound images and its in vivo validation." *Ultrasonics*, vol. 51, no. 2, pp. 181–189, 2011.

[20] S. D. Fenster and J. R. Kender, "Sectored snakes: Evaluating learned-energy segmentations," *IEEE Trans. Pattern Anal. Mach. Intell.*, vol. 23, no. 9, pp. 1028–1034, 2001.

[21] M. A. Charmi, S. Derrode, and F. Ghorbel, "Fourier-based geometric shape prior for snakes," *Pattern Recogn. Lett.*, vol. 29, pp. 897–904, 2008.

[22] R. Ronfard, "Region based strategies for active contour models." *International Journal of Computer Vision*, vol. 13, no. 2, pp. 229–251, 1994.

[23] A. Chakraborty, L. H. Staib, and J. S. Duncan, "Deformable boundary finding in medical images by integrating gradient and region information," *IEEE Transactions on Medical Imaging*, vol. 15, pp. 859–870, 1996.

[24] S. C. Zhu and A. Yuille, "Region competition: Unifying snakes, region growing, and bayes/mdl for multiband image segmentation," *IEEE Transactions on Pattern Analysis and Machine Intelligence*, vol. 18, pp. 884–900, 1996.

[25] T. McInerney and D. Terzopoulos, "T-snakes: Topology adaptive snakes," *Medical Image Analysis*, vol. 4, no. 2, pp. 73–91, 2000.

[26] G. Giraldi, E. Strauss, and A. Oliveira, "Dual-t-snakes model for medical imaging segmentation," *Pattern Recogn. Lett.*, vol. 24, pp. 993–1003, 2003.

[27] H. Delingette, J. Montagnat, and P. Epidaure, "New algorithms for controlling active contours shape and topology," in *European Conference on Computer Vision (ECCV'2000), number 1843 in LNCS*, 2000, pp. 381–395.

[28] H. Delingette and J. Montagnat, "Shape and topology constraints on parametric active contours," *Computer Vision and Image Understanding*, vol. 83, pp. 140–171, 2000.

[29] L. Ji and H. Yan, "Robust topology-adaptive snakes for image segmentation," *Image Vision Comput.*, vol. 20, no. 2, pp. 147–164, 2002.

[30] R. Malladi, J. Sethian, and B. C. Vemuri, "Shape modeling with front propagation: A level set approach," *IEEE Transactions on Pattern Analysis and Machine Intelligence*, vol. 17, pp. 158–175, 1995.

[31] S. Osher and J. Sethian, "Fronts propagating with curvature-dependent speed: Algorithms based on Hamilton-Jacobi formulations," *Journal of Computational Physics*, vol. 79, no. 1, pp. 12–49, Nov. 1988.

[32] V. Caselles, R. Kimmel, and G. Sapiro, "Geodesic active contours," *Int. J. Comput. Vision*, vol. 22, pp. 61–79, 1997.

[33] K. Siddiqi, Y. B. Lauzire, A. Tannenbaum, and S. W. Zucker, "Area and length minimizing flows for shape segmentation," *IEEE Transactions on Image Processing*, vol. 7, pp. 433–443, 1998.

[34] X. Wang, L. He, C. Y. Han, and W. G. Wee, "Deformable contour method: A constrained optimization approach," *INT. J. COMPUT. VISION*, vol. 59, pp. 87–108, 2002.

[35] L. He, Z. Peng, B. Everding, X. Wang, C. Han, K. Weiss, and W. Wee, "A comparative study of deformable contour methods on medical image segmentation," *Image and Vision Computing*, vol. 26, no. 2, pp. 141–163, 2008.

[36] C. Xu, J. L. Prince, and P. D. L., *Medical Image Segmentation Using Deformable Models*, ser. Handbook on Medical Imaging – Volume II: Medical Image Processing and Analysis. SPIE Press, 2000.

[37] C. Li, J. Liu, and M. D. Fox, "Segmentation of external force field for automatic initialization and splitting of snakes," *Pattern Recogn.*, vol. 38, pp. 1947–1960, 2005.

[38] M. Rochery, I. H. Jermyn, and J. Zerubia, "Higher order active contours," *Int. J. Comput. Vision*, vol. 69, pp. 27–42, 2006.

[39] C. Xu and J. L. Prince, "Snakes, shapes, and gradient vector flow," *IEEE Transactions on Image Processing*, vol. 7, no. 3, pp. 359–369, 1998.

[40] C. Xu and J. L. Prince, "Gradient vector flow: a new external force for snakes," in *Proceedings of the international IEEE Computer Society Conference on Computer Vision and Pattern Recognition*, 1997, pp. 66–71.

[41] C. Xu and J. L. Prince, "Generalized gradient vector flow external forces for active contours," *Signal Process.*, vol. 71, no. 2, pp. 131–139, 1998.

[42] M. Wei, Y. Zhou, and M. Wan, "A fast snake model based on non-linear diffusion for medical image segmentation," *Computerized Medical Imaging and Graphics*, vol. 28, no. 3, 2004.

[43] J. Mille, "Narrow band region-based active contours and surfaces for 2d and 3d segmentation," *Comput. Vis. Image Underst.*, vol. 113, pp. 946–965, 2009.

[44] Y. Shang, X. Yang, L. Zhu, R. Deklerck, and E. Nyssen, "Region competition based active contour for medical object extraction," *Comp. Med. Imag. and Graph.*, vol. 32, no. 2, pp. 109–117, 2008.

[45] A. K. Jumaat, W. E. Z. W. A. Rahman, A. Ibrahim, and R. Mahmud, "Segmentation of masses from breast ultrasound images using parametric active contour algorithm," *Procedia - Social and Behavioral Sciences*, vol. 8, pp. 640 – 647, 2010.

[46] T. McInerney, "Sketchsnakes: Sketch-line initialized snakes for efficient interactive medical image segmentation," *Comp. Med. Imag. and Graph.*, vol. 32, no. 5, pp. 331–352, 2008.

[47] G. Hamarneh and T. Gustavsson, "Combining snakes and active shape models for segmenting the human left ventricle in echocardiographic images," in *Computers in Cardiology 2000*, 2000, pp. 115 –118.

[48] C. M. Chen, H. H. S. Lu, and Y. C. Lin, "An early vision-based snake model for ultrasound image segmentation," *Ultrasound in Medicine & Biology*, vol. 26, no. 2, pp. 273 – 285, 2000.

[49] M. Mignotte and J. Meunier, "A multiscale optimization approach for the dynamic contour-based boundary detection issue," *Computerized Medical Imaging and Graphics*, vol. 25, no. 3, pp. 265 – 275, 2001.

[50] A. Rodtook and S. S. Makhanov, "Continuous force field analysis for generalized gradient vector flow field," *Pattern Recognition*, vol. 43, no. 10, pp. 3522 – 3538, 2010.

[51] S. Chucherd and S. S. Makhanov, "Multiresolution phase portrait analysis for segmentation of ultrasound images for detection of breast cancer," *Lecture Notes in Engineering and Computer Science: Proceedings of The International MultiConference of Engineers and Computer Scientists 2011, IMECS 2011*, 16-18 March, 2011, Hong Kong, pp. 460–465.

[52] H. D. Cheng, J. Shan, W. Ju, Y. Guo, and L. Zhang, "Automated breast cancer detection and classification using ultrasound images: A survey," *Pattern Recognition*, vol. 43, no. 1, pp. 299–317, 2010.

[53] O. Michailovich and A. Tannenbaum, "Despeckling of medical ultrasound images," *IEEE Transactions on Ultrasonics Ferroelectrics and Frequency Control*, vol. 53, pp. 64–78, 2006.

[54] C. P. Loizou, C. S. Pattichis, C. I. Christodoulou, R. S. H. Istepanian, M. Pantziaris, and A. Nicolaides, "Comparative evaluation of despeckle filtering in ultrasound imaging of the carotid artery." *IEEE Trans Ultrason Ferroelectr Freq Control*, vol. 52, no. 10, pp. 1653–1669, 2005.

[55] Y. Yu and S. T. Acton, "Speckle reducing anisotropic diffusion," *IEEE Transactions on Image Processing*, vol. 11, no. 11, pp. 1260–1270, 2002.

[56] X. Zhu, P. Zhang, J. Shao, Y. Cheng, Y. Zhang, and J. Bai, "A snake-based method for segmentation of intravascular ultrasound images and its in vivo validation." *Ultrasonics*, vol. 51, no. 2, pp. 181–189, 2010.

[57] Y.-L. Huang, Y.-R. Jiang, D.-R. Chen, and W. K. Moon, "Level set contouring for breast tumor in sonography," *J. Digital Imaging*, vol. 20, no. 3, pp. 238–247, 2007.

[58] B. Levienaise-Obadia and A. H. Gee, "Adaptive segmentation of ultrasound images," *Image Vision Comput.*, vol. 17, no. 8, pp. 583–588, 1999.

[59] J. Yu and J. Tan, "Object density-based image segmentation and its applications in biomedical image analysis," *Comput. Methods Prog. Biomed.*, vol. 96, pp. 193–204, 2009.

[60] L. Vincent, "Morphological grayscale reconstruction in image analysis: Applications and efficient algorithms," *IEEE Transactions on Image Processing*, vol. 2, pp. 176–201, 1993.

[61] A. Baraldi and F. Parmiggiani, "An alternative form of the lee filter for speckle suppression in sar images," *Graph. Models Image Process.*, vol. 57, pp. 75–78, 1995.

[62] S. Gupta, L. Kaur, R. C. Chauhan, and S. C. Saxena, "A versatile technique for visual enhancement of medical ultrasound images," *Digit. Signal Process.*, vol. 17, pp. 542–560, 2007.

[63] A. Lopes, R. Touzi, and E. Nezry, "Adaptive speckle filters and scene heterogeneity," *IEEE Transactions on Geoscience and Remote Sensing*, vol. 28, pp. 992–1000, 1990.

[64] K. Houshmand and H. Tizhoosh, "Increasing segmentation accuracy in ultrasound imaging using filtering and snakes," in *Electrical and Computer Engineering, 2008. CCECE 2008. Canadian Conference on*, may 2008, pp. 1333–1336.

[65] Y. Zhang, R. Sankar, and W. Qian, "Boundary delineation in transrectal ultrasound image for prostate cancer," *Comput. Biol. Med.*, vol. 37, pp. 1591–1599, 2007.

[66] D.-R. Chen, R.-F. Chang, C.-J. Chen, M.-F. Ho, S.-J. Kuo, S.-T. Chen, S.-J. Hung, and W. K. Moon, "Classification of breast ultrasound images using fractal feature," *Clin Imaging*, vol. 29, no. 4, pp. 235–45.

[67] B. Liu, H. D. Cheng, J. Huang, J. Tian, X. Tang, and J. Liu, "Probability density difference-based active contour for ultrasound image segmentation," *Pattern Recogn.*, vol. 43, pp. 2028–2042, 2010.

[68] P. Perona and J. Malik, "Scale-space and edge detection using anisotropic diffusion," *IEEE Transactions on Pattern Analysis and Machine Intelligence*, vol. 12, pp. 629–639, 1990.

[69] R. N. Czerwinski, D. L. Jones, and W. D. O'brien, "Detection of lines and boundaries in speckle images - application to medical ultrasound," *IEEE Transactions on Medical Imaging*, vol. 18, pp. 126–136, 1999.

[70] I. Cohen and I. Herlin, "A motion computation and interpretation framework for oceanographic satellite images," *Computer Vision, International Symposium on*, pp. 13–18, 1995.

[71] X. Tian, S. Samarasinghe, and G. Murphy, "An integrated algorithm for detecting position and size of knots on logs using texture analysis," in *Proceedings of the Conference on Image and Visions Computing*, 1999, pp. 121–132.

[72] J. Li, W.-Y. Yau, and H. Wang, "Combining singular points and orientation image information for fingerprint classification," *Pattern Recogn.*, vol. 41, no. 1, pp. 353–366, 2008.

[73] R. Rangayyan and F. Ayres, "Gabor filters and phase portraits for the detection of architectural distortion in mammograms," *Medical and Biological Engineering and Computing*, vol. 44, pp. 883–894, 2006.

[74] D. Jordan and P. Smith, *Nonlinear ordinary differential equations : an introduction for scientists and engineers / D.W. Jordan and P. Smith*, 4th ed. Oxford ; New York : Oxford University Press, 2007, previous ed.: 1999.

[75] I. Daubechies, *Ten Lectures on Wavelets*, ser. CBMS-NSF Reg. Conf. Series in Applied Math. SIAM, 1992.

[76] N. Saidin, U. K. Ngah, H. A. M. Sakim, D. N. Siong, M. K. Hoe, and I. L. Shuaib, "Density based breast segmentation for mammograms using graph cut and seed based region growing techniques," in *Proceedings of the 2010 Second International Conference on Computer Research and Development*, ser. ICCRD '10, 2010, pp. 246–250.

[77] B. Olstad and A. H. Torp, "Encoding of a priori information in active contour models," *IEEE Trans. Pattern Anal. Mach. Intell.*, vol. 18, pp. 863–872, 1996.

[78] X. D. Zhuang and N. E. Mastorakis, "Region shrinking and image segmentation based on the compressing vector field," in *Proceedings of the 10th WSEAS International Conference on Mathematical Methods and Computational Techniques in Electrical Engineering*, 2008, pp. 217–223.